

Supplementary Material for

Surface reconstruction of tetragonal methylammonium lead triiodide

Azimatu Seidu,<sup>1</sup> Marc Dvorak,<sup>1</sup> Jari Järvi,<sup>1</sup> Patrick Rinke,<sup>1</sup> and Jingrui Li<sup>2</sup>

<sup>1</sup>*Department of Applied Physics, Aalto University, FI-00076 AALTO, Finland*

<sup>2</sup>*Electronic Materials Research Laboratory, Key Laboratory of the Ministry of Education & International Center for Dielectric Research, School of Electronic Science and Engineering, Xi'an Jiaotong University, Xi'an 710049, China*

S1. SURFACE PHASE DIAGRAMS OF  $\text{PbI}_2$ -T SURFACE MODELS

Figure S1 depicts the surface phase diagrams of  $\text{PbI}_2$ -T surface models. The yellow regions show the thermodynamically stable limit for the growth of bulk  $\text{MAPbI}_3$ .

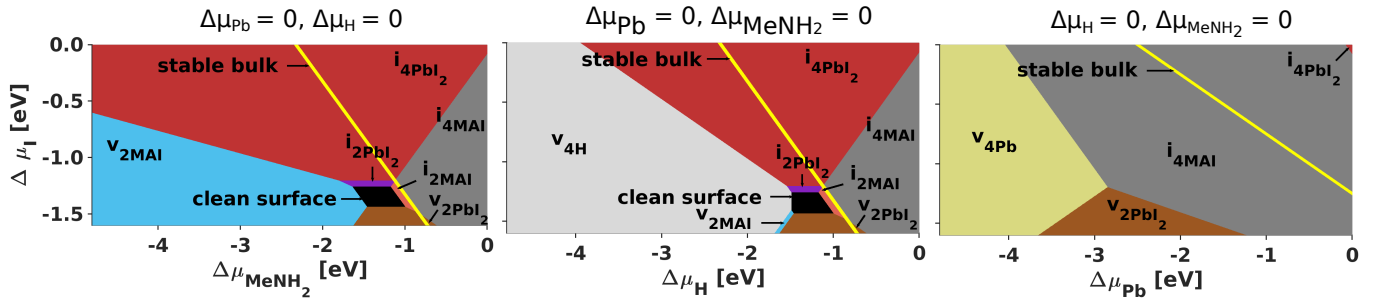


FIG. S1. Surface phase diagrams of reconstructed  $\text{PbI}_2$ -T surface models of tetragonal  $\text{MAPbI}_3$ . The yellow regions depict the thermodynamically stable range for the growth of bulk  $\text{MAPbI}_3$ .

## S2. MOST RELEVANT OPTIMISED RECONSTRUCTED $\text{PbI}_2$ -T SURFACE MODELS

Figure S2 depicts the optimized structures of the most relevant reconstructed  $\text{PbI}_2$ -T surface models. The top panel shows the top view of the topmost atoms with the light gray shades, depicting the topmost octahedra.

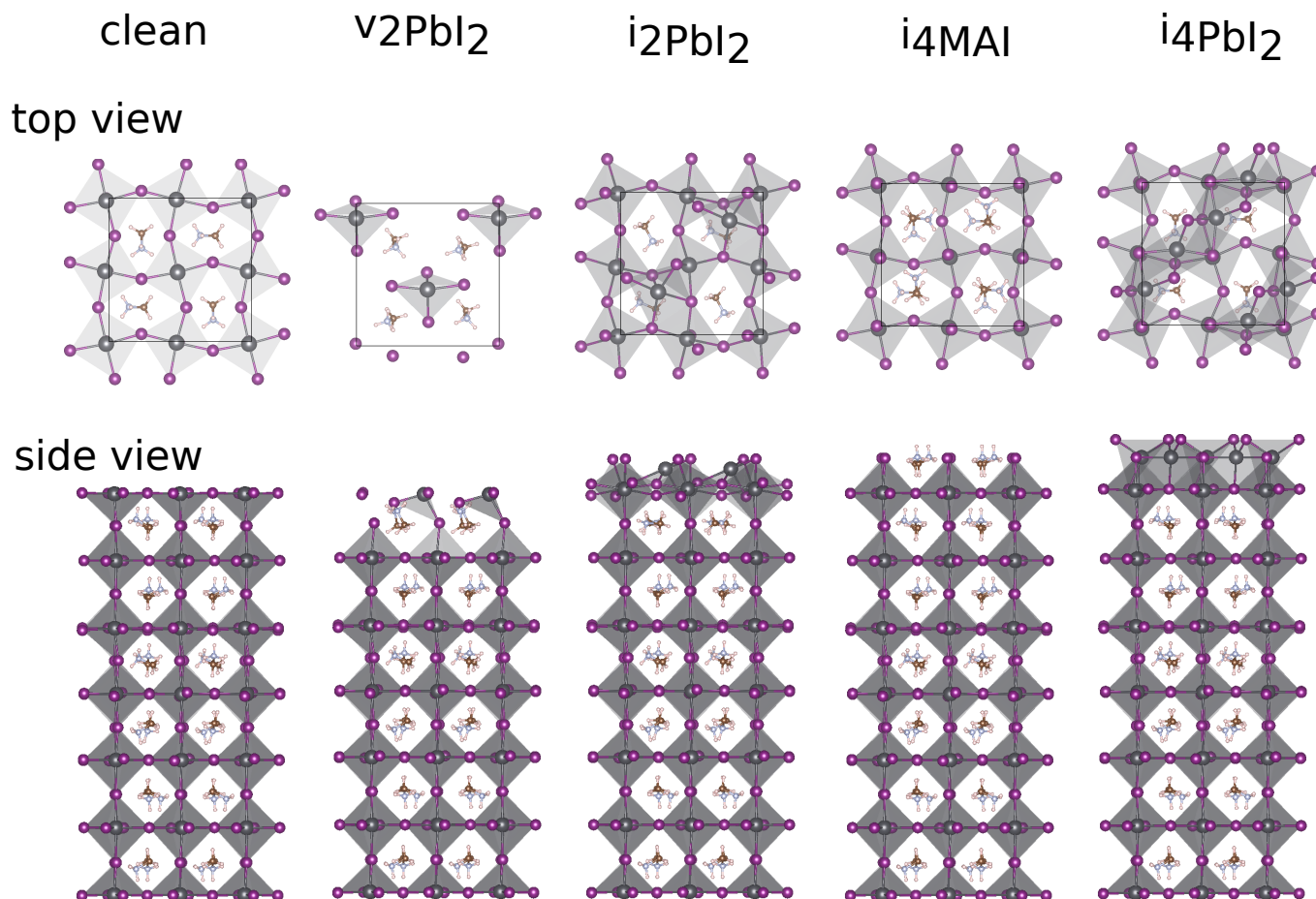


FIG. S2. Optimized crystal structures the most relevant recontruvted  $\text{PbI}_2$ -T surface models of tetragonal  $\text{MAPbI}_3$ .

### S3. BAND STRUCTURE OF THE MOST RELEVANT RECONSTRUCTED SURFACE MODELS WITH $\text{PbI}_2$ -T

Band structures of the most relevant reconstructed surface model with  $\text{PbI}_2$ -terminations are shown in Fig. S3. The valence band maximum is set to zero and depicted with the red line. The projected bulk band structure is included as blue shading for comparison.

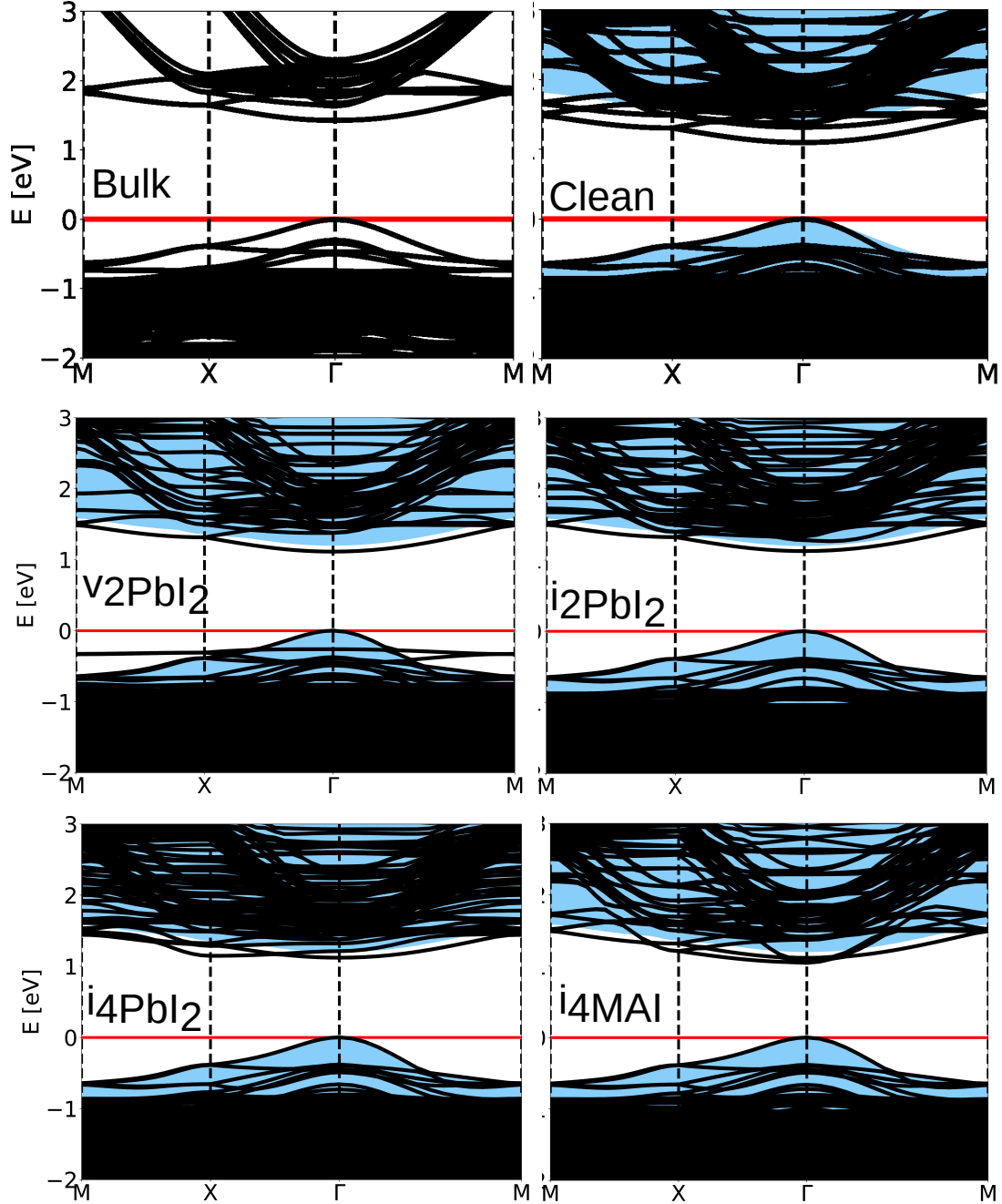


FIG. S3. Band structures of bulk and the most relevant reconstructed  $\text{PbI}_2$ -T surface models of  $\text{MAPbI}_3$ . In the surface band structure plots, the projected bulk band structure is shown as blue shading. The red line depicts the valence band maximum (VBM).

# Surface reconstruction of tetragonal methylammonium lead triiodide

Azimatu Seidu,<sup>1, a)</sup> Marc Dvorak,<sup>1</sup> Jari Järvi,<sup>1</sup> Patrick Rinke,<sup>1</sup> and Jingrui Li<sup>2</sup><sup>1)</sup>*Department of Applied Physics, Aalto University, FI-00076 AALTO, Finland*<sup>2)</sup>*Electronic Materials Research Laboratory, Key Laboratory of the Ministry of Education & International Center for Dielectric Research, School of Electronic Science and Engineering, Xi'an Jiaotong University, Xi'an 710049, China*

(Dated: 28 February 2022)

We present a detailed first-principles analysis of the (001) surface of methylammonium lead triiodide (MAPbI<sub>3</sub>). With density-functional theory we investigate the atomic and electronic structure of the tetragonal (*I4cm*) phase of MAPbI<sub>3</sub>. We analysed surfaces models with MAI- (MAI-T) and PbI<sub>2</sub>-terminations (PbI<sub>2</sub>-T). For both terminations, we studied the clean-surface and a series of surface reconstructions. We find that the clean MAI-T model is more stable than its PbI<sub>2</sub>-T counterpart. For the MAI termination, reconstructions with added or removed units of nonpolar MAI and PbI<sub>2</sub> are most stable. The corresponding band structures reveal surface states originating from the conduction band. Despite the presence of such additional surface states, our stable reconstructed surface models do not introduce new states within the band gap.

## I. INTRODUCTION

Perovskite solar cells (PSCs) have attracted immense attention within the photovoltaic community due to their rapidly rising power conversion efficiency (PCE): it reached 25.5%<sup>1</sup> only nine years after the invention of the state-of-the-art PSC architecture in 2012 (PCE ~10%)<sup>2,3</sup>. The hybrid (organic-inorganic) halide perovskite (HP) methylammonium (MA) lead triiodide (CH<sub>3</sub>NH<sub>3</sub>PbI<sub>3</sub> or MAPbI<sub>3</sub>) has been the most common PSC photoabsorber for a long time, and it is still a major focus of both experimental and theoretical studies, along with the rising isostructural material based on formamidinium (FA). HPs have also received significant recognition in luminescence and light detection<sup>4-9</sup>.

To advance HPs for eventual use in large-scale commercial applications, further efforts in fundamental research are still necessary to enable materials and device engineering. Researching surface passivation is critical in this regard since defects at perovskite surfaces and grain boundaries are centers of nonradiative recombination, which is a major inhibitor to further PCE improvement<sup>10-16</sup>. Additionally, organic components in hybrid HPs suffer from rapid degradation when exposed to moisture, heat, and oxygen<sup>17-22</sup>, the effects of which can be reduced with proper surface passivation. To enhance the stability of HPs and enable large-scale applications, measures need to be taken to mitigate their instability with minimal compromise to PCE. Several proposals have addressed this challenge. Notable approaches include surface passivation via organic long-chain ligands<sup>23-25</sup>, dimensionality reduction of perovskite active materials<sup>26-31</sup>, protective coating with inorganic semiconductors or insulators<sup>32-35</sup>, and A-site substitution with smaller monovalent ions<sup>36-43</sup>.

The application of these proposed solutions requires

an understanding of the surface properties and possible surface reconstructions of HPs. This includes several aspects, such as morphology control during the growth of the HP thin films, HP-interlayer interface engineering, and the passivation of intrinsic defects at the interfaces and grain boundaries. A comprehensive understanding of the atomic and electronic structure of MAPbI<sub>3</sub> surfaces would advance the development of this class of novel materials and their applications. The surfaces of MA-<sup>44-47</sup> and FA-based<sup>48-50</sup> perovskites have been investigated theoretically and experimentally<sup>4,51-58</sup>, but understanding of the non-pristine surfaces is still lacking. Most of the MA-perovskite surface studies are focused on the stability of the two main terminations of HP (001) surfaces: MAI- and PbI<sub>2</sub>-terminated (shortened as MAI-T and PbI<sub>2</sub>-T hereafter, respectively) with little to no consideration of possible surface reconstructions.

In our previous work, we investigated the atomic and electronic structure of (001) surfaces of cesium lead triiodide (CsPbI<sub>3</sub>) using first-principles density functional theory (DFT) calculations and surface-phase-diagram (SPD) analysis<sup>59</sup>. For both cubic ( $\alpha$ ) and orthorhombic ( $\gamma$ ) phases, we found that the CsI-termination is more stable than PbI<sub>2</sub>-termination, and the former class features a series of stable surface reconstructions with added or removed valence-neutral CsI and PbI<sub>2</sub> units. Our previous study established a systematic method for understanding stable surface reconstructions with a representative HP and motivates the present work in regard to both materials engineering and theoretical methodology.

In this work, we present a comprehensive DFT study of the (001) surface of the room-temperature tetragonal phase of the more popular HP, MAPbI<sub>3</sub>. Haruyama et al. have carried out preliminary studies for this surface and identified some stable surface terminations dependent on growth conditions, with some of them beyond the regular “clean surface” models<sup>44,45</sup>. Nevertheless, an extensive exploration of surface terminations and reconstructions with the addition or removal of constituent elements CH<sub>3</sub>NH<sub>2</sub> (MeNH<sub>2</sub>), Pb, I, and their complexes is lacking.

<sup>a)</sup>Electronic mail: [azimatu.seidu@aalto.fi](mailto:azimatu.seidu@aalto.fi)

We aim to establish such a systematic theoretical description by means of DFT, *ab initio* thermodynamics<sup>60–62</sup>, and SPD analysis.

It is worth noting that the unique charge state of the organic MA cation introduces additional complexity into this DFT study compared to our work on CsPbI<sub>3</sub>. Simply separating MAPbI<sub>3</sub> into its constituents MA, Pb, and I in a way similar to the decomposition of CsPbI<sub>3</sub> into Cs, Pb, and I<sub>2</sub> is not thermodynamically sensible. The charge-neutral CH<sub>3</sub>NH<sub>3</sub> radical is not stable on its own and far less suitable as a thermodynamic reference system than Cs is for CsPbI<sub>3</sub>. We therefore use the neutral CH<sub>3</sub>NH<sub>2</sub> (MeNH<sub>2</sub>) and H<sub>2</sub> molecules in this work. Similar to Ref. 59, we will classify the thermodynamic stability of considered MAPbI<sub>3</sub> surfaces for different growth conditions and analyze their electronic structure.

The remainder of this paper is organized as follows. In Sec. II, we briefly outline the computational details of our DFT calculations and summarize the thermodynamic constraints for the growth of bulk MAPbI<sub>3</sub>, as well as the MAI-T and PbI<sub>2</sub>-T surfaces. In Sec. III, we first analyze the stability of the clean-surface models (MAI-T and Pb<sub>2</sub>-T) and the reconstructed models with missing- and add-atoms and complexes. We then discuss the impact of surface reconstruction on both the atomic and electronic structure. Finally, we conclude with a summary in Sec. IV.

## II. COMPUTATIONAL DETAILS

All DFT calculations were performed using the Perdew-Burke-Ernzerhof exchange-correlation functional for solids (PBEsol)<sup>63</sup> implemented in the all-electron numeric-atom-centered orbital code FHI-AIMS<sup>64–66</sup>. We chose PBEsol because it describes the lattice constants of MAPbI<sub>3</sub> well at moderate computational cost<sup>67,68</sup>. In our previous study on CsPbI<sub>3</sub> surfaces<sup>59</sup>, we also tested the PBE functional, but found only negligible changes in the surface phase diagram. We expect the same to be true for MAPbI<sub>3</sub>. Scalar relativistic effects were included by means of the zeroth-order regular approximation<sup>69</sup>. As with the PBE test, the inclusion of full spin-orbit coupling did not affect the conclusions of our CsPbI<sub>3</sub> study<sup>59</sup> and we expect the same for MAPbI<sub>3</sub>. Standard FHI-AIMS tier-2 basis sets were used in combination with  $\Gamma$ -centered  $4 \times 4 \times 4$  (bulk) and  $4 \times 4 \times 1$  (surfaces)  $k$ -point meshes. The bulk structures were optimized with the analytical stress tensor<sup>70</sup> until forces were below  $5.0 \times 10^{-3} \text{ eV} \cdot \text{\AA}^{-1}$ . For the surface slab models, we fixed the lattice constants and all atomic positions except for atoms in the top and bottom MAPbI<sub>3</sub> units (the surface atoms). A surface-dipole correction<sup>71</sup> was applied in all surface calculations.

In the interest of open science<sup>72</sup>, we made all relevant calculations included in this work available on the Novel Materials Discovery (NOMAD) repository<sup>73</sup>.

## A. Structural optimization

### 1. Bulk and surface structures

As experimentally reported, the tetragonal phase of MAPbI<sub>3</sub> is stable from  $\sim 160$  to  $\sim 330$  K, including room temperature<sup>74,75</sup>. The structure belongs to the polar space group  $I4cm$  (No. 108) as a result of its intrinsic polarization along the principal axis<sup>74</sup>. Considering several possible disordered MA alignments<sup>76,77</sup>, we constructed a series of  $2 \times 2 \times 2$  supercells with different MA orientations and optimized their structures with DFT. We then take the structure with the lowest energy. The lattice parameters of this structure (Fig. 1) are  $a = b = 12.40 \text{ \AA}$ ,  $c = 12.68 \text{ \AA}$ . Figure 1 displays some disorder and an overall vertical (downward in the side view, i.e.,  $[00\bar{1}]$ ) net dipole, which is formed by the C–N dipoles of the MA cations. The horizontal, i.e., (001), component of the overall dipole moment within the model nearly vanishes.

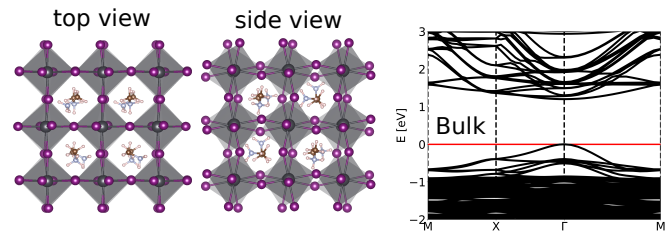


FIG. 1. Bulk geometry and band structure of  $I4cm$  phase of CH<sub>3</sub>NH<sub>3</sub>PbI<sub>3</sub> in the  $2 \times 2 \times 2$  supercell model. C, H, N, Pb, and I are colored in brown, light gray, light blue, black, and purple, respectively. The PbI<sub>6</sub> octahedra are colored in dark gray. The valence band maximum is set to zero and depicted by the red line in the band structure plot.

In this work, we focus on the (001) surfaces, which are the major facet of HPs<sup>44,45,78</sup> and the most relevant surfaces of MAPbI<sub>3</sub>. Due to the polar bulk structure, it is not possible to build a surface supercell by repeating several bulk layers along the  $[001]$  direction as this would result in a polar surface model (see Figure 2a left). Such a model will induce artefacts into the calculated properties of the system such as the unphysical removal of band degeneracies and reduction of the band gap (Fig. 2a right) and would ultimately lead to a polar catastrophe, in which the valence band at one end of the slab lie higher in energy than the conduction bands at the other end.

To circumvent these artefacts, we constructed a symmetric slab model by introducing a “domain wall” in the slab. As sketched in Figure 2b left, such a domain wall is a PbI<sub>2</sub>-containing (001) plane located at the center of the slab. The atomic structures on opposite sides of the domain wall is mirrored with respect to this plane, so that the  $[001]$  components of the MA dipole moments on opposite sides cancel each other, giving rise to a nearly vanishing overall dipole moment. As a result, the polar artefacts vanish and the surface band structure (Fig. 2b right) exhibits a proper band gap and the right degeneracies. Similar approaches have been successfully employed

in previous studies<sup>44,79</sup>.

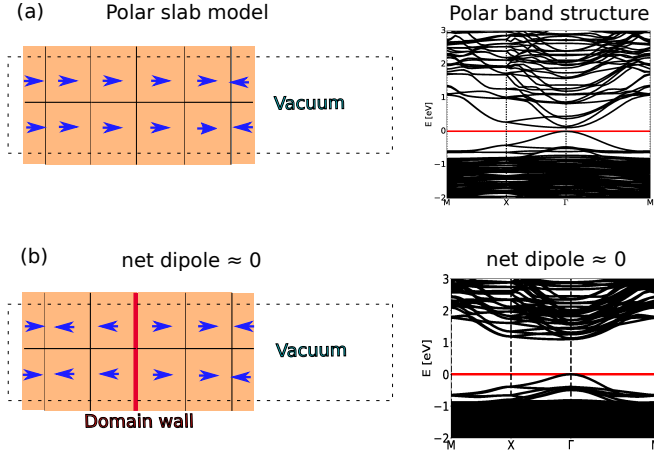


FIG. 2. Construction of nonpolar MAI-T slab model, with the [001] components of MA dipoles represented by blue arrows. (a) A polar slab model results from simple repetition of bulk unit cells. (b) By mirroring bulk structures around a central domain wall, the overall dipole vanishes. Also shown is how the surface dipoles on both sides of the slab reorient themselves during relaxation and point inwards as a result of hydrogen bonding with surface I ions. The band structure of each model is given in the right column.

With the approach illustrated in Fig. 2b, we constructed symmetric clean surface models in a way similar to our previous work for CsPbI<sub>3</sub>. Specifically, the MAI-T surface model consists of 6 MAI and 5 PbI<sub>2</sub> layers alternately stacked along the [001] direction. Similarly, the PbI<sub>2</sub>-T surface model has 7 PbI<sub>2</sub> and 6 MAI alternating layers. By inserting a 40 Å-thick vacuum layer to separate neighboring slabs along [001] and including surface-dipole correction<sup>71</sup> in the DFT calculations, we minimized the interaction between neighboring slabs.

Figure 3 depicts the optimized structures of both clean MAI-T and PbI<sub>2</sub>-T surfaces. The top views of both phases show a similar in-plane tilting pattern of PbI<sub>6</sub> octahedra and in-plane alignment of MA dipoles as in the bulk. The side views demonstrate that the mirror symmetry of both slab models with respect to the domain wall is maintained after geometry optimization. We note that in MAI-T, MA dipoles at both top and bottom surfaces point inwards (sketched in Fig. 2) as a result of hydrogen bonding with the surface I ions.

We studied various add- and missing-atom surface models based on both MAI-T and PbI<sub>2</sub>-T clean surfaces. All add-atom models ( $i_X$ ) were constructed by adding the atoms or atom-complexes X to the surface, while for missing-atom models ( $v_X$ ), atoms or complexes X were removed from the topmost X-containing layers. For MAI-T surfaces as an example,  $v_{MeNH_2}$ ,  $v_H$ ,  $v_{MA}$ ,  $v_I$ , and  $v_{MAI}$  were constructed by removing atoms from the topmost MAI layer, while  $v_{Pb}$  and  $v_{PbI_2}$  indicate the removal of atoms from the PbI<sub>2</sub> layer below the topmost MAI layer. For models with double missing- or add-atoms (i.e.,  $v_{2X}$  or  $i_{2X}$ ), we considered both line and diag-

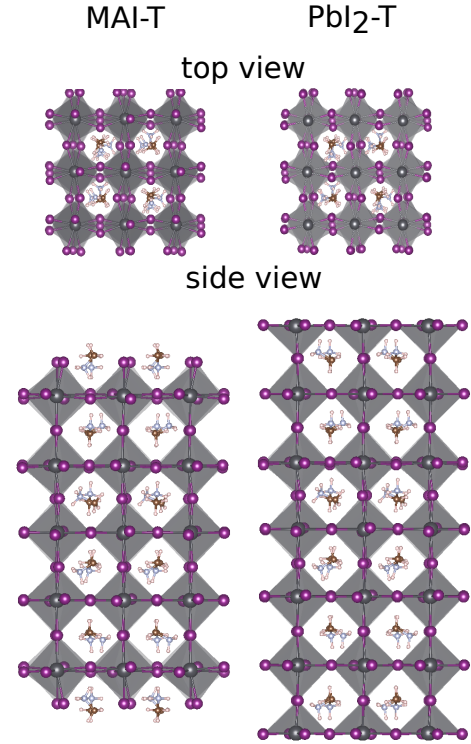


FIG. 3. Relaxed MAI-T and PbI<sub>2</sub>-T clean-surface models. Depicted on the left is the MAI-T and on the right the PbI<sub>2</sub>-T termination.

onal modes that correspond to the reconstruction units distributed along the [100] or [110] directions, respectively. Only the more stable model will be presented and discussed in Sec. III. For instance, we find the line modes to be more stable in both  $v_{2MAI}$  and  $i_{2PbI_2}$ .

TABLE I. Reconstructed MAI-T and PbI<sub>2</sub>-T surface models of tetragonal MAPbI<sub>3</sub> considered in this work.

MAI-T		PbI <sub>2</sub> -T	
$v_{MeNH_2}$	$i_{MeNH_2}$	$v_{MeNH_2}$	$i_{MeNH_2}$
$v_{2MeNH_2}$	$i_{2MeNH_2}$	$v_{2MeNH_2}$	$i_{2MeNH_2}$
$v_{MA}$	$i_{MA}$	$v_{MA}$	$i_{MA}$
$v_{2MA}$	$i_{2MA}$	$v_{2MA}$	$i_{2MA}$
$v_{4MA}$	$i_{Pb}$	$v_{Pb}$	$i_{Pb}$
$v_{Pb}$	$i_{2Pb}$	$v_{2Pb}$	$i_{2Pb}$
$v_{2Pb}$	$i_I$	$v_{4Pb}$	$i_I$
$v_I$	$i_{2I}$	$v_I$	$i_{2I}$
$v_{2I}$	$v_H$	$v_{2I}$	$i_H$
$v_H$	$i_{2H}$	$v_H$	$i_{2H}$
$v_{2H}$	$i_{4H}$	$v_{2H}$	$i_{4H}$
$v_{4H}$	$i_{MAI}$	$v_{4H}$	$i_{MAI}$
$v_{MAI}$	$i_{2MAI}$	$v_{MAI}$	$i_{2MAI}$
$v_{2MAI}$	$i_{4MAI}$	$v_{2MAI}$	$i_{4MAI}$
$v_{4MAI}$	$i_{PbI_2}$	$v_{PbI_2}$	$i_{PbI_2}$
$v_{PbI_2}$	$i_{2PbI_2}$	$v_{2PbI_2}$	$i_{2PbI_2}$
$v_{2PbI_2}$	$i_{4PbI_2}$	$v_{4PbI_2}$	$i_{4PbI_2}$

## B. Thermodynamic constraints for stable MAPbI<sub>3</sub> bulk and surfaces

We applied the grand potential analysis to investigate the stability of a variety of different surface reconstructions. Neglecting finite temperature contributions, the grand potential ( $\Omega$ ) is

$$\Omega = \Delta H - \sum_i x_i \Delta \mu_i = E - \sum_i x_i \mu_i^\ominus - \sum_i x_i \Delta \mu_i. \quad (1)$$

Here,  $\Delta H$  indicates the standard formation energy of the model system,  $E$  the total energy,  $\mu_i^\ominus$  the chemical potential of species  $i$  in its most stable form,  $x_i$  the number of atoms of this species in the structure, and  $\Delta \mu_i$  the change in the chemical potential away from its value in the element's most stable phase,  $\mu_i^\ominus$ .  $\Delta \mu_i$  represents the control of experimental growth conditions and is both a meaningful and convenient parameter to vary in phase diagrams. The relative stability between two structures is determined by comparing their grand potentials, with the structure lower in grand potential considered more stable. Details of the grand potential analysis are described in our previous work on surface reconstruction of CsPbI<sub>3</sub><sup>59</sup>.

We first consider conditions for stable MAPbI<sub>3</sub> in the bulk. In order to avoid the formation of elemental Pb and I, molecular MA (as a whole instead of elemental C, N, and H for simplicity), as well as bulk MAI and PbI<sub>2</sub>, the region of the phase diagram for stable MAPbI<sub>3</sub> is determined by the inequalities,

$$\begin{aligned} \Delta H(\text{MAPbI}_3) &\leq \Delta \mu_{\text{MA}} \leq 0, \\ \Delta H(\text{MAPbI}_3) &\leq \Delta \mu_{\text{Pb}} \leq 0, \\ \Delta H(\text{MAPbI}_3) &\leq 3\Delta \mu_{\text{I}} \leq 0; \end{aligned}$$

and

$$\begin{aligned} \Delta H(\text{MAPbI}_3) &\leq \Delta \mu_{\text{MA}} + \Delta \mu_{\text{Pb}} + 3\Delta \mu_{\text{I}}, \\ \Delta \mu_{\text{MA}} + \Delta \mu_{\text{I}} &\leq \Delta H(\text{MAI}), \\ \Delta \mu_{\text{Pb}} + 2\Delta \mu_{\text{I}} &\leq \Delta H(\text{PbI}_2). \end{aligned}$$

However, due to the unstable radical nature of neutral MA  $\equiv$  CH<sub>3</sub>NH<sub>3</sub> (the reaction CH<sub>3</sub>NH<sub>2</sub> +  $\frac{1}{2}$ H<sub>2</sub>  $\rightarrow$  CH<sub>3</sub>NH<sub>3</sub> is endothermic), we use the sum ( $\mu_{\text{MeNH}_2}^\ominus + \mu_{\text{H}}^\ominus$ ) instead of  $\mu_{\text{MA}}^\ominus$ , and similarly ( $\Delta \mu_{\text{MeNH}_2} + \Delta \mu_{\text{H}}$ ) instead of  $\Delta \mu_{\text{MA}}$ . The inequalities should then be rewritten as

$$\begin{aligned} \Delta H(\text{MAPbI}_3) &\leq \Delta \mu_{\text{MeNH}_2} \leq 0, \\ \Delta H(\text{MAPbI}_3) &\leq \Delta \mu_{\text{H}} \leq 0, \\ \Delta H(\text{MAPbI}_3) &\leq \Delta \mu_{\text{Pb}} \leq 0, \\ \Delta H(\text{MAPbI}_3) &\leq 3\Delta \mu_{\text{I}} \leq 0; \end{aligned} \quad (2)$$

and

$$\begin{aligned} \Delta H(\text{MAPbI}_3) &\leq \Delta \mu_{\text{MeNH}_2} + \Delta \mu_{\text{H}} \\ &\quad + \Delta \mu_{\text{Pb}} + 3\Delta \mu_{\text{I}}, \\ \Delta \mu_{\text{MeNH}_2} + \Delta \mu_{\text{H}} + \Delta \mu_{\text{I}} &\leq \Delta H(\text{MAI}), \\ \Delta \mu_{\text{Pb}} + 2\Delta \mu_{\text{I}} &\leq \Delta H(\text{PbI}_2). \end{aligned} \quad (3)$$

The inequalities in Eq. (3) can be rearranged as

$$\begin{aligned} \Delta H(\text{MAPbI}_3) - \Delta H(\text{MAI}) &\leq \Delta \mu_{\text{Pb}} + 2\Delta \mu_{\text{I}} \\ &\leq \Delta H(\text{PbI}_2), \\ \Delta H(\text{MAPbI}_3) - \Delta H(\text{PbI}_2) &\leq \Delta \mu_{\text{MeNH}_2} + \Delta \mu_{\text{H}} + \Delta \mu_{\text{I}} \\ &\leq \Delta H(\text{MAI}). \end{aligned} \quad (4)$$

Inequalities in Eq. (2) define the domains of variables  $\mu_{\text{MeNH}_2}$ ,  $\mu_{\text{H}}$ ,  $\mu_{\text{Pb}}$ , and  $\mu_{\text{I}}$ , and the inequalities in Eq. (4) define the region for growth of “stable-bulk MAPbI<sub>3</sub>” in the phase diagram.  $\mu_{\text{MeNH}_2}^\ominus$ ,  $\mu_{\text{H}}^\ominus$ ,  $\mu_{\text{Pb}}^\ominus$ , and  $\mu_{\text{I}}^\ominus$  can be calculated for the stable reference structures of MeNH<sub>2</sub> (molecule), H (H<sub>2</sub> molecule), Pb (*P6<sub>3</sub>/mmc*), and I (I<sub>2</sub> molecule) with DFT, respectively. Formation energies  $\Delta H$  in Eq. (4) can be calculated with DFT, too.

Equations (2) and (4) only serve to determine the bulk stability. For the stability of (clean and reconstructed) surface models, we need to solve Eq. (1) to obtain the SPDs. Note that the bulk and surface are not in isolation from each other. The final surface stability is determined by the intersection of the SPD and the stable-bulk region.

In principle, we need to plot the SPDs in four dimensions (4D) as the grand potential of each surface is a function of four variables ( $\Delta \mu_{\text{MeNH}_2}$ ,  $\Delta \mu_{\text{H}}$ ,  $\Delta \mu_{\text{Pb}}$ , and  $\Delta \mu_{\text{I}}$ ). In practice, however, such a 4D diagram is hard to draw and visualize, and we use three two-dimensional (2D) slices instead: the  $\Delta \mu_{\text{I}}/\Delta \mu_{\text{MeNH}_2}$  slice at  $\Delta \mu_{\text{Pb}} = \Delta \mu_{\text{H}} = 0$ , the  $\Delta \mu_{\text{I}}/\Delta \mu_{\text{Pb}}$  slice at  $\Delta \mu_{\text{MeNH}_2} = \Delta \mu_{\text{H}} = 0$ , and the  $\Delta \mu_{\text{I}}/\Delta \mu_{\text{H}}$  slice at  $\Delta \mu_{\text{Pb}} = \Delta \mu_{\text{MeNH}_2} = 0$ .

## III. RESULTS AND DISCUSSION

### A. Thermodynamic stability analysis of bulk and surface terminations

The PBEsol-calculated formation energies of bulk MAPbI<sub>3</sub>, MAI, and PbI<sub>2</sub> are  $-4.82$ ,  $-2.30$ , and  $-2.47$  eV, respectively. From Eq. (4), we can find the numerical values for thermodynamic growth limits of bulk MAPbI<sub>3</sub> in its tetragonal phase:

$$\begin{aligned} -2.53 \text{ eV} &\leq \Delta \mu_{\text{Pb}} + 2\Delta \mu_{\text{I}} \leq -2.47 \text{ eV}, \\ -2.35 \text{ eV} &\leq \Delta \mu_{\text{MeNH}_2} + \Delta \mu_{\text{H}} + \Delta \mu_{\text{I}} \leq -2.30 \text{ eV}. \end{aligned}$$

The energy required for tetragonal MAPbI<sub>3</sub> to decompose into MAI and PbI<sub>2</sub>, i.e., the difference between the left and the right values of either inequality, is as small as 0.06 eV. Such a narrow stability region reflects the general instability of tetragonal MAPbI<sub>3</sub>.

SPD analysis helps identify the stability of the two considered surface terminations. Figure 4 shows that, at  $\Delta \mu_{\text{MeNH}_2} = \Delta \mu_{\text{H}} = 0$ , the MAI-T and PbI<sub>2</sub>-T clean surfaces are stable in the Pb-poor and Pb-rich limits, respectively. We consider MAI-T the more stable surface since the region for stable MAI-T covers a wider range of

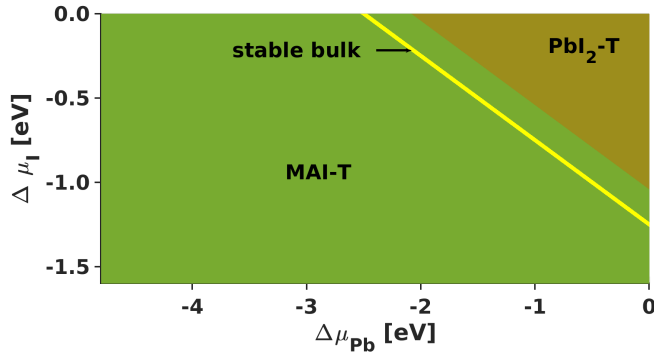


FIG. 4. Thermodynamic growth limit for MAI-T and  $\text{PbI}_2$ -T surfaces in tetragonal  $\text{MAPbI}_3$ . The yellow shaded regions depict the thermodynamically stable range for the growth of bulk  $\text{MAPbI}_3$ .

$\Delta\mu_k$  ( $k = \text{Pb}$  and  $\text{I}$ , as well as  $\text{MeNH}_2$  and  $\text{H}$  which are not shown here). Furthermore and quite importantly, the stable bulk region, shown by yellow shading in Figure 4, intersects only the MAI-T surface. This finding agrees with previous theoretical results for  $\text{MAPbI}_3$ <sup>10,58,80–83</sup> that claimed the stability of MAI-T over  $\text{PbI}_2$ -T and is similar to the  $\text{CsPbI}_3$  surface properties that we reported earlier<sup>59</sup>. Our discussions will therefore focus on MAI-T surfaces from here on. Data for  $\text{PbI}_2$ -T surfaces, including the relaxed surface-reconstructions and the SPDs, are given in the Supplementary Material (SM).

## B. Identification of stable reconstructions of MAI-T surfaces

SPDs for the considered surface reconstructions of the MAI-T surfaces are shown in Figure 5 (SPDs for the  $\text{PbI}_2$ -T counterparts are available in Fig. S1 of SM). It is not surprising that the  $\Delta\mu_{\text{I}}/\Delta\mu_{\text{MeNH}_2}$  and  $\Delta\mu_{\text{I}}/\Delta\mu_{\text{H}}$  SPDs display similar features, as  $\text{MeNH}_2$  and  $\text{H}$  are closely related to each other through the organic MA component of the material. In these two SPDs, which are given in the Pb-rich limit ( $\Delta\mu_{\text{Pb}} = 0$ ), we observe the following stable surface structures:  $i_{4\text{MAI}}$  (in the  $\text{MeNH}_2$ - and H-rich limit),  $v_{4\text{MAI}}$  (in the  $\text{MeNH}_2$ - and H-poor limit), clean surface,  $v_{\text{PbI}_2}$ ,  $v_{2\text{PbI}_2}$ ,  $i_{\text{PbI}_2}$ ,  $i_{2\text{PbI}_2}$ ,  $i_{2\text{MAI}}$ , and  $v_{\text{MAI}}$ . The major difference in the appearance of these two phase diagrams lies with the  $v_{4\text{H}}$  surface, which is observed in the H-poor and I-rich limit. With our choice of 2D slices, this surface reconstruction appears in one quadrant of only one of these two 2D phase diagrams.

The  $\text{MeNH}_2$ - and H-rich (thus MA-rich) limit ( $\Delta\mu_{\text{MeNH}_2} = \Delta\mu_{\text{H}} = 0$ ) creates a third 2D slice of the total phase diagram, shown on the right side of Figure 5. In this SPD, we find  $i_{4\text{MAI}}$  and  $v_{2\text{PbI}_2}$  to be stable. Except for  $v_{4\text{H}}$ , all the observed stable reconstructions are valence-neutral, i.e., with addition or removal of MAI or  $\text{PbI}_2$  units, net charges are not induced in the system, which is similar to what we previously found for the

$\text{CsPbI}_3$  surfaces<sup>59</sup>. We notice that in the  $\text{MeNH}_2$ -, H-, and Pb-rich limit  $i_{4\text{MAI}}$  dominates over  $\text{PbI}_2$ -derived reconstructions. That is, on the MAI termination layer at the  $\text{MAPbI}_3$  surface, the tendency for growing an extra MAI layer is greater than for growth of  $\text{PbI}_2$  units, which would eventually transform the system into  $\text{PbI}_2$ -T. This finding again verifies that MAI-T is more stable.

We are particularly interested in the most relevant reconstructions, which we define as those regions in the SPDs that intersect the stable bulk region. It is these overlapping regions of bulk and surface stability that are viable standalone surfaces in the laboratory. These relevant models are the clean surface,  $v_{\text{PbI}_2}$ ,  $v_{2\text{PbI}_2}$ ,  $i_{\text{PbI}_2}$ , and  $i_{2\text{PbI}_2}$  in the Pb-rich limit, and  $i_{4\text{MAI}}$  in the MA-rich limit. Different from  $\text{CsPbI}_3$ , for which we observe a relatively broad range in chemical potential for the clean surface, the range for its stability on MAI-T (001) at  $\Delta\mu_{\text{Pb}} = 0$  is very narrow in terms of  $\Delta\mu_{\text{MeNH}_2}$  and  $\Delta\mu_{\text{H}}$ . In addition, it is only stable in I-deficient growth conditions.

The optimized geometries of the most relevant surface models are given in Figure 6 (relevant reconstruction models of  $\text{PbI}_2$ -T are presented in Fig. S2 of SM). Because the surface atomic structure varies mainly to accommodate the absence or addition of atoms, our discussion of geometric rearrangement will be with reference to the clean surface in the following. We observe that  $\text{PbI}_2$  removal causes noticeable atomic structure changes in the reconstructed surfaces. The topmost  $\text{PbI}_2$  layer of  $v_{\text{PbI}_2}$  displays  $(\text{PbI}_6)_2(\text{PbI}_5)$  polyhedra, while in  $v_{2\text{PbI}_2}$  there are two isolated  $\text{PbI}_5$  polyhedra (Fig. 7). Interestingly, no migration of surface I anions occurs in  $v_{2\text{PbI}_2}$ , which is the main characteristic of the equivalent removal on  $\alpha$ - $\text{CsPbI}_3$ <sup>59</sup>. This is very likely due to the different A-site cations: the hydrogen bonding between the ammonium group and the surface I anions would stabilize the latter, so that the surface Pb-I units are relatively regularly distributed.

In  $i_{\text{PbI}_2}$  and  $i_{2\text{PbI}_2}$ , each added  $\text{PbI}_2$  unit is linked to a surface I atom via Pb-I bonding, giving rise to a  $\text{PbI}_3$  tetrahedron that contains one Pb and three I atoms as its vertices (Figure 7). Notably, the  $i_{2\text{PbI}_2}$  reconstruction shows characteristic  $\text{PbI}_5\text{PbI}_3$  polyhedra (Fig. 7), as previously reported by Haruyama et al.<sup>44</sup>. This asymmetric distribution of surface I atoms results from the removal of two linearly-aligned  $\text{PbI}_2$  units, which is very different to the same surface reconstruction of  $\alpha$ - $\text{CsPbI}_3$  where the diagonal mode is more stable.

Finally, we find a relatively regular alignment of the added MAI units, forming a uniform sheet on the MAI-T surface in  $i_{4\text{MAI}}$ . The C-N bonds of all added  $\text{MA}^+$  cations point towards the surface to form hydrogen bonds with the topmost I anions. The average shortest  $\text{H}(\text{N}) \cdots \text{I}$  distance is 2.68 Å, a typical value for hydrogen bonding<sup>84,85</sup>. The fact that extra MAI units can readily grow above the already existing MAI surface-termination layer, as also indicated by the SPDs in Fig. 5, makes it very likely that MAI multilayers can grow on  $\text{MAPbI}_3$



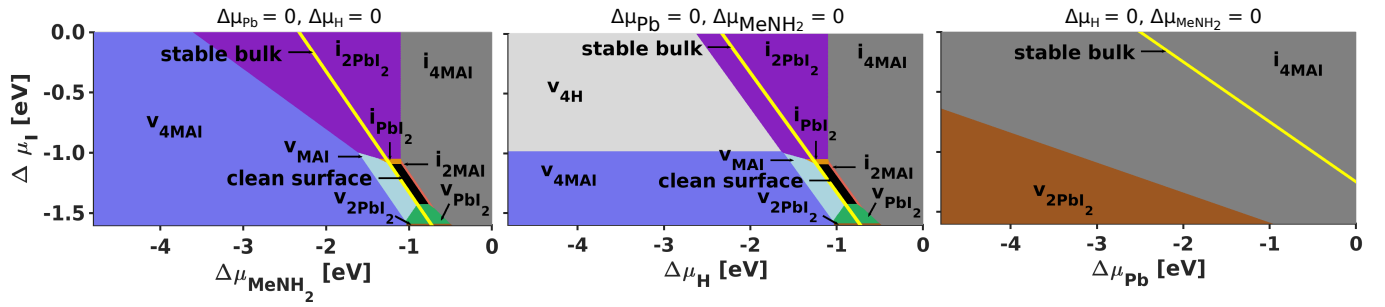


FIG. 5. 2D slices through the 4 dimensional surface phase diagrams of MAI-T surfaces of tetragonal MAPbI<sub>3</sub>. The yellow regions in each panel marks the bulk stability region of MAPbI<sub>3</sub>.

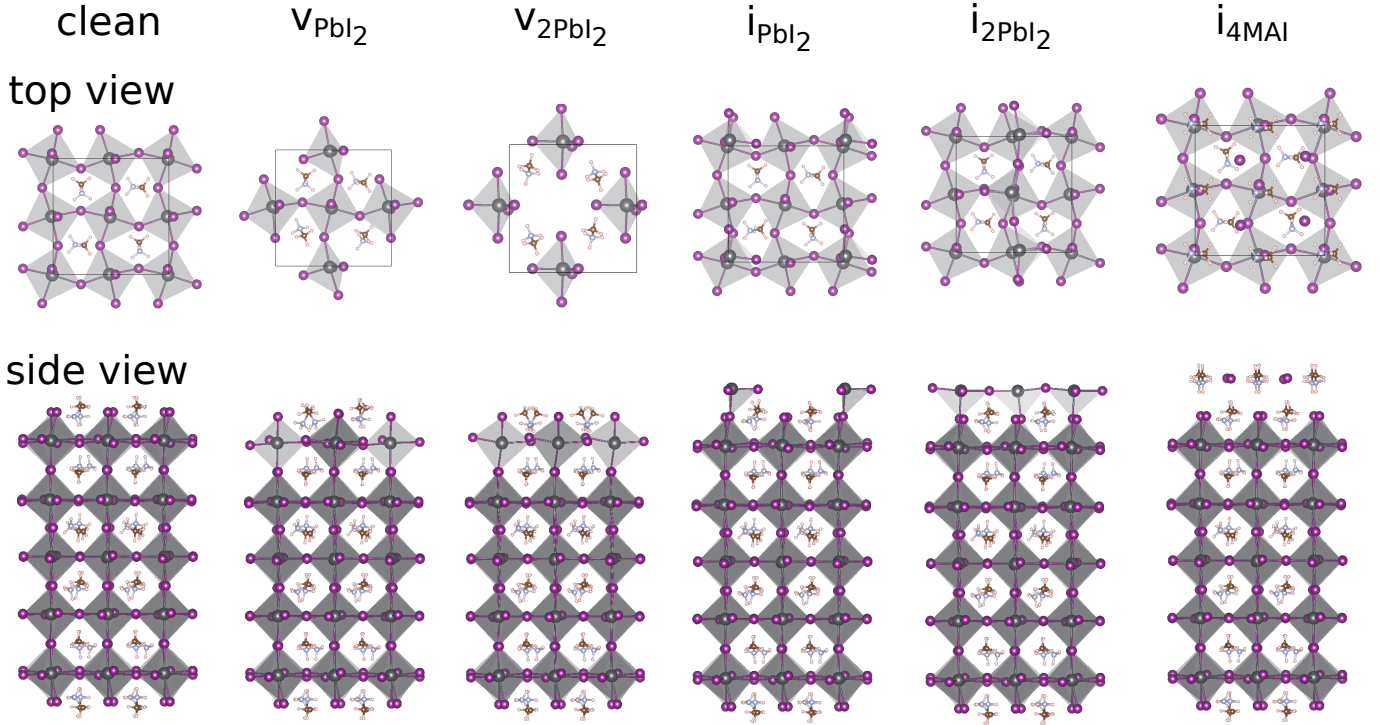


FIG. 6. Atomic structures of the most relevant surface reconstruction models of tetragonal MAPbI<sub>3</sub>. The atomic colour convention follows that of Fig. 1. The light gray shades depict the octahedra in the topmost in the “top view” and sites with missing or add PbI<sub>2</sub>-units in the “side view”.

surfaces in MAI-rich situations. This would be detrimental to device performance since MAI is very poor in transporting charge carriers.

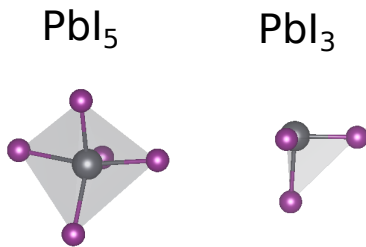


FIG. 7. Surface polyhedra in reconstructed models with missing- and add-PbI<sub>2</sub> units.

### C. Electronic properties of bulk and most relevant reconstructed MAPbI<sub>3</sub> surface models

In this section, we focus on the electronic properties of bulk MAPbI<sub>3</sub> and the most relevant reconstructed MAI-T surface models. The band structures of the most relevant PbI<sub>2</sub>-T surface reconstructions are presented in Fig. S3 of SM.

#### 1. Electronic properties of the bulk and the clean MAI-T surface

Figure 8 depicts the band structures of the bulk and the pristine MAI-T surface of MAPbI<sub>3</sub>. For the bulk, we adopt the high-symmetry *k*-point path of a simple-cubic

lattice in the  $2 \times 2 \times 2$  supercell model for simplicity. Our plots show the band structure along  $M-X-\Gamma-M$  with  $M = (\frac{1}{2}, \frac{1}{2}, 0)$ ,  $X = (0, \frac{1}{2}, 0)$ , and  $\Gamma = (0, 0, 0)$ , i.e., within the  $a^*b^*$  plane of the Brillouin zone (identical to the  $ab = (001)$  plane in real space in our cases).

The bulk band structure exhibits a direct band gap at the  $\Gamma$  point. The element projected density of states (PDOS) in Fig. 9 reveals that the valence band (VB) is dominated by I-5*p* orbitals. The VB maximum (VBM) exhibits a noticeable contribution from Pb-6*s* which gives rise to the well-known antibonding character and thus introduces the noticeable band dispersion at  $\Gamma$  (Fig. 8). The conduction-band minimum (CBM) consists mainly of Pb-6*p* orbitals. The MA cation shows no significant contributions at the band edges.

Next, we investigate, if our MAI-T surface model introduces surface or mid-gap states. The bands of the clean MAI-T surface are shown in the middle panel of Fig. 8. Both the VB and CB edges of the surface nearly align with the bulk bands at the M point. The band gap of the surface at M is slightly larger than the bulk, which could be a quantum confinement artefact of the slab model, but the bands themselves agree. At  $\Gamma$  and X, however, the CB of the clean surface extends below the CBM of the bulk. At these points, the shapes of the bulk and surface bands at  $\Gamma$  are different.

To understand the nature of these states, we first analyse the PDOS in Fig. 9. The PDOS verifies that the apparent band gap of the clean surface is  $\sim 0.2$  eV less than the bulk, as already indicated by the band structure. We plot the charge densities of the lowest four CB states of our surface model in Fig. 10. We find that these states are surface states that come in nearly degenerate pairs, with the partners of each pair on opposite sides of the slab. The slight degeneracy lift in each pair is caused by a small relaxation induced structural asymmetry in the two bulk halves that make up our surface slab model (see Section II A 1). The characters of these band edge wave functions are the same as the ones we observed for the  $\alpha$  phase of CsPbI<sub>3</sub><sup>59</sup>.

The DOS of the clean surface in Fig. 9 is consistent with the interpretation of conduction band derived surface states. The right panel exhibits small bumps as shown by the arrow in Fig. 9 (right panel) in the CB at approximately 1.25 and 2.10 eV compared to the bulk, indicating the rearrangement of bands in the slab model.

The behaviour of the VBM is a little different. It is pinned to the domain wall at the mid-plane of the slab model. This quasi-two-dimensional state is still dispersive and its band very closely matches that of the bulk, which provides good evidence for the quality of our slab model. The pinning of the state to the mid-plane is reasonable. The dipoles on either side of the domain wall point away from the mid-plane, raising the energy of an electron residing on the mid-plane and positioning it as the maximum of the occupied states (VBM). Again, the lack of artefacts in the slab electronic structure and good agreement with the bulk support the quality of the

model, even with the pinning of the VBM to the domain wall.

## 2. Electronic properties of the most relevant MAI-T surface models

The band structure and PDOS of the most relevant surface models observed in Fig. 5, ( $v_{\text{PbI}_2}$ ,  $v_{2\text{PbI}_2}$ ,  $i_{\text{PbI}_2}$ ,  $i_{2\text{PbI}_2}$ , and  $i_{4\text{MAI}}$ ), are shown in Figures 11 and 12, respectively. Similar to Fig. 8, the bulk band structure is included as background for comparison in Fig. 11. We find that the band structures of two of the most relevant reconstructed surface models,  $v_{\text{PbI}_2}$  and  $i_{4\text{MAI}}$ , resemble the band structure of the clean MAI-T surface shown in Fig. 8.

For the others, there are flat bands near and below the bulk CB edges (CBEs), which are more pronounced at the M-point. They are most visible in  $i_{\text{PbI}_2}$ . In the  $i_{\text{PbI}_2}$  and  $i_{2\text{PbI}_2}$  surfaces, we observe increased intensities within the CB of the PDOS at  $\sim 1.6$  and  $\sim 1.9$  eV, which corresponds to the flat bands at M-point in Fig. 11. These small peaks come from Pb states, suggesting that the flat bands are indeed due to the added PbI<sub>2</sub> units. To confirm this, we plot the charge distribution of CBE at M for these two reconstructions in Figure 13.

Even though the CBE at M in these two reconstructions and in  $v_{2\text{PbI}_2}$  belongs to a band which is flat across the entire Brillouin zone, the wave functions of these states (Fig. 13) still resemble the surface states of the pristine slab, especially for  $v_{2\text{PbI}_2}$  and  $i_{2\text{PbI}_2}$ . This is somewhat surprising since the CBE states of the clean-surface model belong to a dispersive band. The CBE states of the reconstructed surfaces in Fig. 13 still come in nearly degenerate pairs with each partner appearing on opposite sides of the slab, as for the clean surface. However, we can ignore the state at the bottom of the slab, since it corresponds to the clean and not the reconstructed surface. The states in  $i_{\text{PbI}_2}$  and  $i_{2\text{PbI}_2}$  at the top of the slab, on the reconstructed surface side, have considerable weight on the added PbI<sub>2</sub> units. This wave-function localization explains the flat character of the band.

## IV. CONCLUSION

In summary, we have investigated the stability and electronic structure of MAPbI<sub>3</sub> surfaces in the tetragonal phase from first principles. To circumvent the polar catastrophe in our supercell calculations, we build a slab geometry from two MAPbI<sub>3</sub> bulk segments with opposite polarity, effectively introducing a domain wall in the middle of the slab. Our surface science study reveals that the methylammonium-iodine (MAI) termination is more stable than the PbI<sub>2</sub> termination. We further observe that the removal or addition of polar units that induce

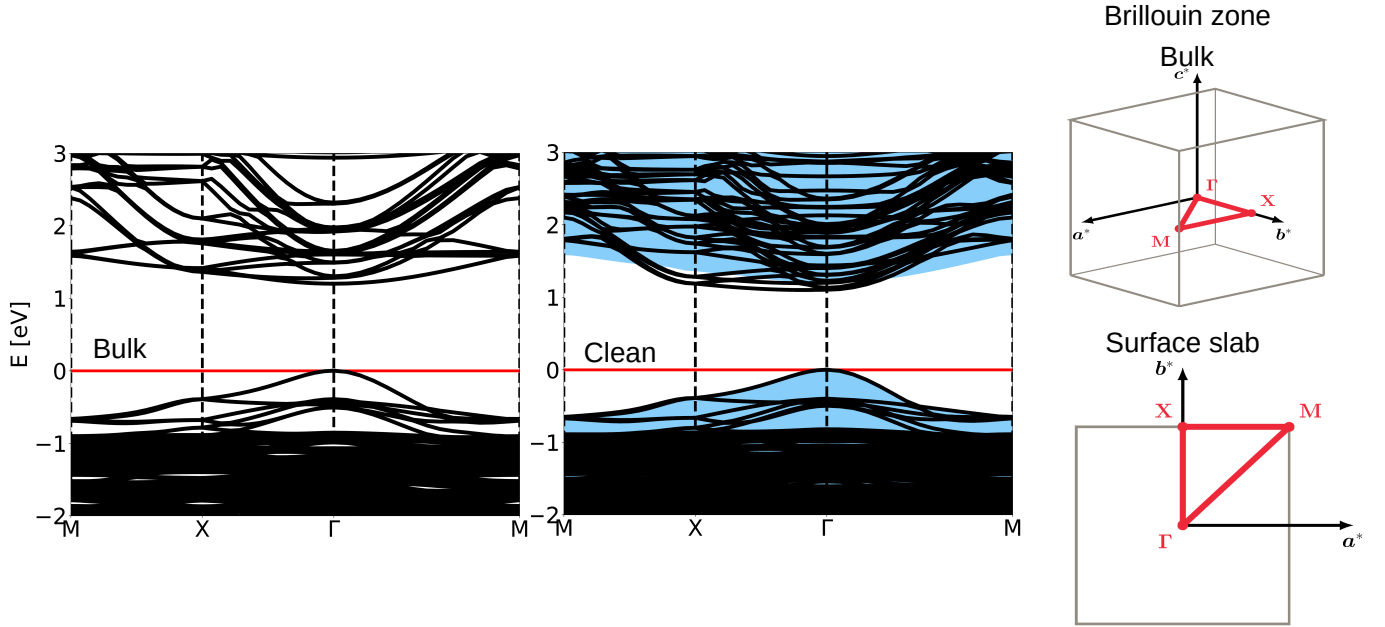


FIG. 8. Band structures of bulk and clean MAI-T surface of tetragonal  $\text{MAPbI}_3$ . Both bulk and surface band structures are calculated with a  $2 \times 2$  in-plane supercell to share a common Brillouin zone and  $k$ -point path (far right). VBM is set to 0 as marked by the red horizontal line. In the surface band structure plots, the projected bulk band structure is shown as blue shading.

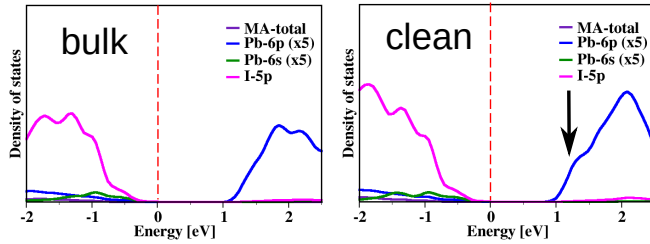


FIG. 9. Density of states of the bulk and clean MAI-T surface of tetragonal  $\text{MAPbI}_3$ , showing the contributions of different atomic species. We scaled the Pb density of states by a factor 5 (depicted by \*5) to make it more visible. The arrow is indicative of the surface states at the edge of the CB in the clean surface.

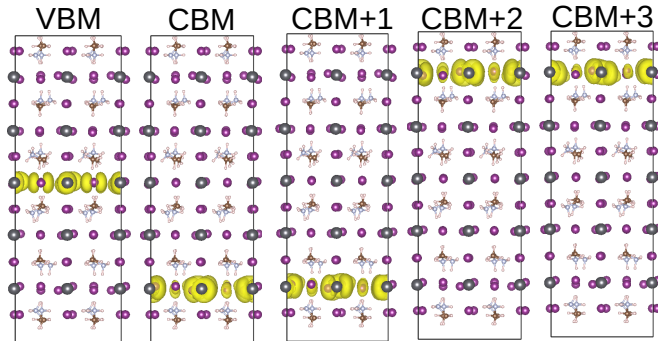


FIG. 10. Charge distributions of the valence band maximum (VBM) and conduction band minimum (CBM) up to CBM+3 at  $\Gamma$  point for the clean surface.

zero net charge in the system lead to more stable sur-

face reconstructions. MAI-terminated surfaces introduce conduction-band derived surface states near the conduction band edge, which result in a surface band gap that is slightly smaller than the bulk band gap. The stable reconstructions do not introduce further surface states in the band gap, which bodes well for the transport properties across interfaces with these reconstructions. Our study opens up future work on surface adsorbates, defects and interfaces.

## V. SUPPLEMENTARY MATERIAL

See Supplementary Material for surface phase diagrams of  $\text{PbI}_2$ -terminated models, crystal and electronic band structures of the most relevant reconstructed surfaces of  $\text{PbI}_2$ -T models.

## VI. AUTHORS CONTRIBUTIONS

All authors contributed equally in this work.

## ACKNOWLEDGMENTS

We acknowledge the computing resources from the CSC-IT Center for Science, the Aalto Science-IT project, and Xi'an Jiaotong University's HPC Platform. We further acknowledge funding from the Väisälä Foundation and the Academy of Finland through its Key

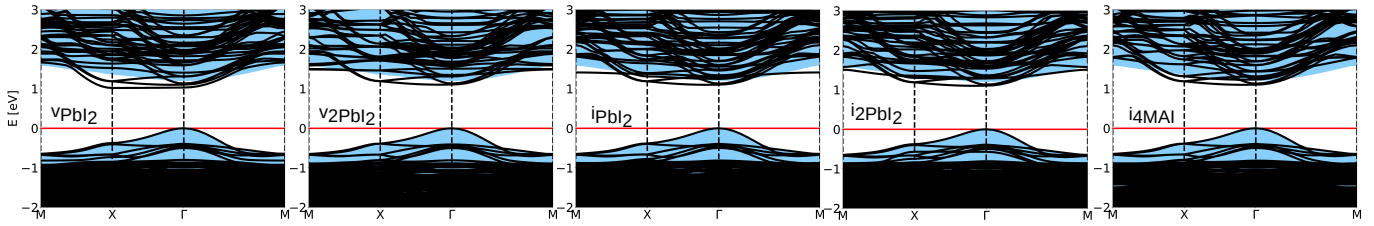


FIG. 11. Band structures of the most relevant surface reconstruction models in tetragonal MAPbI<sub>3</sub>. The bulk-projected band structure is depicted by the blue shading.

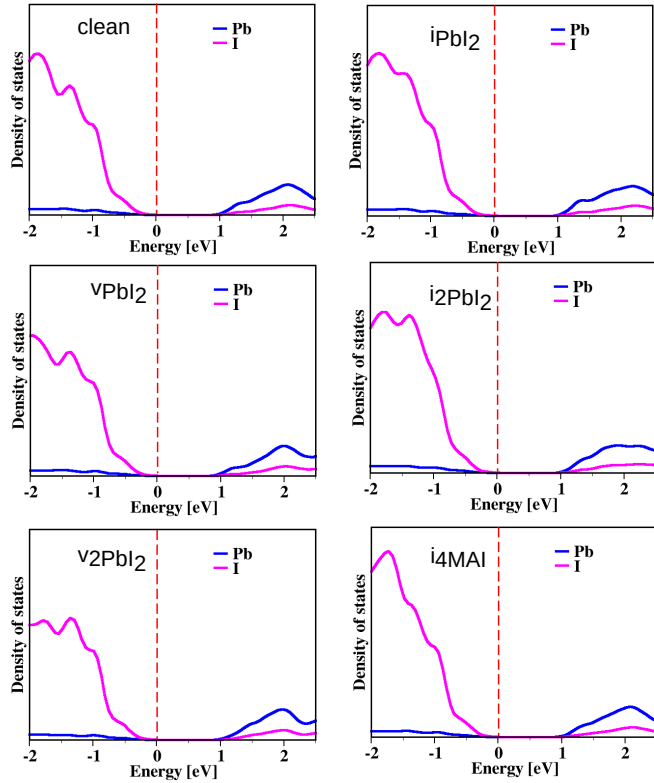


FIG. 12. Density of states of the most relevant surface reconstruction models in MAI-T tetragonal MAPbI<sub>3</sub>. The VBM is set to zero and shown as a red dashed line.

Project Funding scheme (305632) and postdoctoral grant no. 316347.

## VII. CONFLICT OF INTEREST

The authors have no conflicts to disclose.

## VIII. AIP PUBLISHING DATA SHARING POLICY

The data that supports the findings of this study will be openly available in Novel Materials Discovery (NO-MAD) repository at <sup>73</sup>.

<sup>1</sup><https://www.nrel.gov/pv/assets/pdfs/best-research-cell-efficiencies.20200311.pdf>

(National Renewable Energy Laboratory: Best research-cell efficiencies, 2020).

<sup>2</sup>H.-S. Kim, C.-R. Lee, J.-H. Im, K.-B. Lee, T. Moehl, A. Marchioro, S.-J. Moon, R. Humphry-Baker, J.-H. Yum, J. E. Moser, M. Grätzel, and N.-G. Park, “Lead Iodide Perovskite Sensitized All-Solid-State Submicron Thin Film Mesoscopic Solar Cell with Efficiency Exceeding 9%,” *Sci. Rep.* **2**, 591 (2012).

<sup>3</sup>M. M. Lee, J. Teuscher, T. Miyasaka, T. N. Murakami, and H. Snaith, “Efficient hybrid solar cells based on Meso-Structured organometal halide perovskites,” *Science* **338**, 643 (2012).

<sup>4</sup>C. Das, M. Wussler, T. Hellmann, T. Mayer, I. Zimmermann, C. Maheu, M. K. Nazeeruddin, and W. Jaegermann, “Surface, interface and bulk electronic and chemical properties of complete perovskite solar cells: Tapered cross-section photoelectron spectroscopy, a novel solution,” *Appl. Mater. Interfaces* **12**, 40949–409571 (2020).

<sup>5</sup>P. Giulia, “Highly efficient perovskite leds,” *Nature Rev. Mat.* **6**, 2058 (2021).

<sup>6</sup>L.-Y. Huang and W. R. L. Lambrecht, “Lattice dynamics in perovskite halides SnX<sub>3</sub> with X = I, Br, Cl,” *Phys. Rev. B* **90**, 195201 (2014).

<sup>7</sup>Q. Lin, A. Armin, D. M. Lyons, P. L. Burn, and P. Meredith, “Low Noise, IR-Blind Organohalide Perovskite Photodiodes for Visible Light Detection and Imaging,” *Advanced Materials* **27**, 2060–2064 (2015).

<sup>8</sup>H. Cho, S.-H. Jeong, M.-H. Park, Y.-H. Kim, C. Wolf, C.-L. Lee, J. H. Heo, A. Sadhanala, N. Myoung, S. Yoo, S. H. Im, R. H. Friend, and T.-W. Le, “Overcoming the electroluminescence efficiency limitations of perovskite light-emitting diodes,” *Science* **350**, 1222 (2015).

<sup>9</sup>C. Li, H. Wang, F. Wang, T. Li, M. Xu, H. Wang, Z. Wang, X. Zhan, W. Hu, and L. Shen, “Ultrafast and broadband photodetectors based on perovskite/organic bulk heterojunction for large-dynamic-range imaging,” *Light: Science and Applications* **31**, 1–8 (2020).

<sup>10</sup>W.-J. Yin, T. Shi, and Y. Yan, “Unusual defect physics in CH<sub>3</sub>NH<sub>3</sub>PbI<sub>3</sub> perovskite solar cell absorber,” *Appl. Phys. Lett.* **104**, 063903 (2014).

<sup>11</sup>K. X. Steirer, P. Sculz, G. Teeter, V. Stevanovic, M. Yang, K. Zhu, and J. J. Berry, “Defect tolerance in methylammonium lead triiodide perovskite,” *ACS Energy Lett.* **1**, 360–366 (2016).

<sup>12</sup>A. Walsh, D. O. Scanlon, S. Chen, X. G. Gong, and S.-H. Wei, “Self-regulation mechanism for charged point defects in hybrid halide perovskites,” *Angew. Chem. Int. Ed.* **54**, 1791 (2015).

<sup>13</sup>J. Kim, S.-H. Lee, J. H. Lee, and K.-H. Hong, “The role of intrinsic defects in methylammonium lead iodide perovskite,” *J. Phys. Chem. Lett.* **5**, 1312–1317 (2014).

<sup>14</sup>J. M. Ball and A. Petrozza, “Defects in perovskite-halides and their effects in solar cells,” *Nat. Energy* **1**, 16149 (2016).

<sup>15</sup>X. Wu, M. T. Trinh, D. Niesner, H. Zhu, Z. Norman, J. S. Owen, O. Yaffe, B. J. Kudisch, and X. Y. Zhu, “Trap states in lead iodide perovskites,” *J. Am. Chem. Soc.* **137**, 2089–2096 (2015).

<sup>16</sup>R. Long, J. Liu, and O. V. Prezhdo, “Unravelling the Effects of Grain Boundary and Chemical Doping on Electron–Hole Recom-

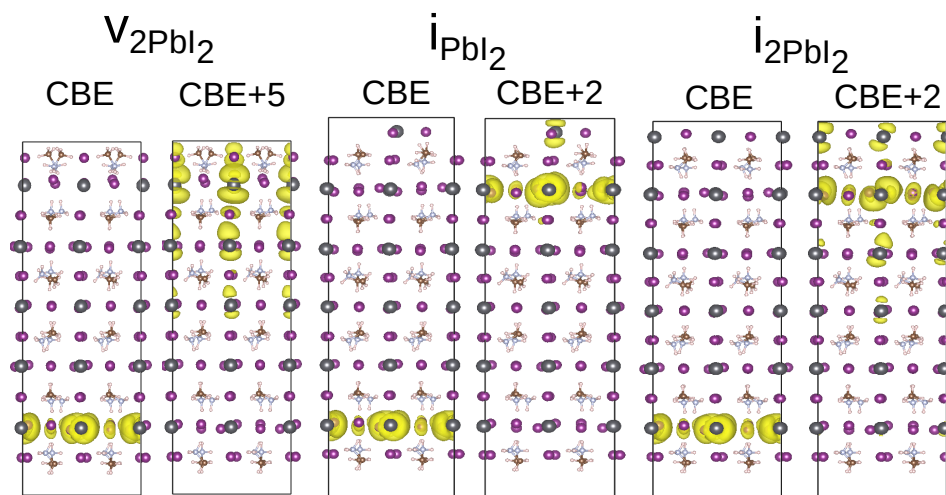


FIG. 13. Charge distribution for  $v_{2PbI_2}$ ,  $i_{PbI_2}$  and  $i_{2PbI_2}$  of the conduction band edges (CBE) at M-point. We also show CBE+5  $v_{2PbI_2}$  as well as CBE+2 for  $i_{PbI_2}$  and  $i_{2PbI_2}$ .

- bination in  $CH_3NH_3PbI_3$  Perovskite by Time-Domain Atomistic Simulation," *J. Am. Chem. Soc.* **138**, 3884 (2016).
- <sup>17</sup>G. Niu, W. Li, F. Meng, L. Wang, H. Dong, and Y. Qiu, "Study on the stability of  $CH_3NH_3PbI_3$  films and the effect of post-modification by aluminumoxide in all-solid-state hybrid solar cells," *J. Mater. Chem. A* **2**, 705 (2014).
- <sup>18</sup>G. Niu, X. Guo, and L. Wang, "Review of recent progress in chemical stability of perovskite solar cells," *J. Mater. Chem. A* **3**, 8970 (2015).
- <sup>19</sup>J. Huang, S. Tan, P. D. Lund, and H. Zhou, "Impact of  $H_2O_2$ ," *Energy Environ. Sci.* **10**, 2284 (2017).
- <sup>20</sup>G.-H. Kim, H. Jang, Y. J. Yoon, J. Jeong, S. Y. Park, B. Walker, I.-Y. Jeon, Y. Jo, H. Yoon, M. Kim, J.-B. Baek, D. S. K, and J. Y. Kim, "Fluorine functionalized graphene nano platelets for highly stable inverted perovskite solar cells," *Nano Lett.* **17**, 6385 (2017).
- <sup>21</sup>I. Mesquita, L. Andrade, and A. Mendes, "Perovskite solar cells: Materials, configurations and stability," *Renew. Sustain. Energy Rev.* **82**, 2471 (2018).
- <sup>22</sup>F. Li, J. Yuan, X. Ling, Y. Zhang, Y. Yang, S. H. Cheung, C. H. Y. Ho, X. Gao, and W. Ma, "A universal strategy to utilize polymeric semiconductors for perovskite solar cells with enhanced efficiency and longevity," *Adv. Funct. Mater.* **28**, 1706377 (2018).
- <sup>23</sup>L. C. Schmidt, A. Pertegá, S. González-Carrero, O. Malinkiewicz, S. Agouram, G. M. Espallargas, H. J. Bolink, R. E. Galian, and J. Pérez-Prieto, "Nontemplate Synthesis of  $CH_3NH_3PbBr_3$  Perovskite Nanoparticles," *J. Am. Chem. Soc.* **136**, 850 (2014).
- <sup>24</sup>S. González-Carrero, R. E. Galian, and J. Pérez-Prieto, "Maximizing the emissive properties of  $CH_3NH_3PbBr_3$  perovskite nanoparticles," *J. Mater. Chem. A* **3**, 9187 (2015).
- <sup>25</sup>H. Dong, J. Xi, L. Zuo, J. Li, Y. Yang, D. Wang, Y. Yu, L. Ma, C. Ran, W. Gao, B. Jiao, J. Xu, T. Lei, F. Wei, F. Yuan, L. Zhang, Y. Shi, X. Hou, and Z. Wu, "Conjugated molecules "bridge": Functional ligand toward highly efficient and long-term stable perovskite solar cell," *Adv. Funct. Mater.* **29**, 1808119 (2019).
- <sup>26</sup>L. N. Quan, M. Yuan, R. Comin, O. Voznyy, E. M. Beauregard, S. Hoogland, A. Buin, A. R. Kirmani, K. Zhao, A. Amassian, D. H. Kim, and E. H. Sargent, "Ligand-stabilized reduced-dimensionality perovskites," *J. Am. Chem. Soc.* **138**, 2649 (2016).
- <sup>27</sup>L. Dou, "Emerging two-dimensional halide perovskite nanomaterials," *J. Mater. Chem. C* **5**, 11165 (2017).
- <sup>28</sup>C. Ran, J. Xi, W. Gao, F. Yuan, T. Lei, B. Jiao, X. Hou, and Z. Wu, "Bilateral interface engineering toward efficient 2D-3D bulk heterojunction tin halide lead-free perovskites solar cells," *ACS Energy Lett.* **3**, 713 (2018).
- <sup>29</sup>Z. Wang, A. M. Ganose, C. Niu, and D. O. Scanlon, "First-principles insights into tin-based two-dimensional hybrid halide perovskites for photovoltaics," *J. Mater. Chem. A* **6**, 5652 (2018).
- <sup>30</sup>C. Liu, W. Huhn, K.-Z. Du, A. Vazquez-Mayagoitia, D. Dirkes, W. You, Y. Kanai, D. B. Mitzi, and V. Blum, "Tunable Semiconductors: Control over Carrier States and Excitations in Layered Hybrid Organic-Inorganic Perovskite," *Phys. Rev. Lett.* **121**, 146401 (2018).
- <sup>31</sup>C. Ran, W. Gao, J. Li, J. Xi, L. Li, J. Dai, Y. Yang, X. Gao, H. Dong, B. Jiao, I. Spanopoulos, C. D. Malliakas, X. Hou, M. G. Kanatzidis, and Z. Wu, "Conjugated organic cations enable efficient self-healing  $FASnI_3$  solar cells," *Joule* **3**, 3072 (2019).
- <sup>32</sup>F. Matteocci, L. Cinà, E. Lamanna, S. Cacovich, G. Divitini, P. A. Midgley, C. Ducati, and A. di Carlo, "Encapsulation for long-term stability enhancement of perovskite solar cells," *Nano Energy* **30**, 162 (2016).
- <sup>33</sup>R. Cheacharoen, N. Rolston, D. Harwood, K. A. Bush, R. H. Dauskardt, and M. D. McGehee, "Design and understanding of encapsulated perovskite solar cells to withstand temperature cycling," *Energy Environ. Sci.* **11**, 144 (2018).
- <sup>34</sup>R. Cheacharoen, C. C. Boyd, G. F. Burkhard, T. Leijtens, J. A. Raiford, K. A. Bush, S. F. Bent, and M. D. McGehee, "Encapsulation for long-term stability enhancement of perovskite solar cells," *Sustain. Energy Fuels* **2**, 2398 (2018).
- <sup>35</sup>A. Seidu, L. Himanen, J. Li, and P. Rinke, "Database-driven high-throughput study of coating materials for hybrid perovskites," *New J. Phys.* **21**, 083018 (2019).
- <sup>36</sup>J. H. Noh, S. H. Im, J. H. Heo, T. N. Mandal, and S. I. Seok, "Chemical Management for Colourful, Efficient, and Stable Inorganic-Organic Hybrid Nanostructured Solar Cells," *Nano Lett.* **13**, 1764 (2013).
- <sup>37</sup>C. Yi, J. Luo, S. Meloni, A. Boziki, N. Ashari-Astani, C. Grätzel, S. M. Zakeeruddin, U. Röthlisberger, and M. Grätzel, "Entropic stabilization of mixed A-cation  $ABX_3$  metal halide perovskites for high performance perovskite solar cells," *Energy Environ. Sci.* **9**, 656 (2016).
- <sup>38</sup>Y. Zhou, Z. Zhou, M. Chen, Y. Zong, J. Huang, S. Pang, and N. P. Padture, "Doping and alloying for improved perovskite solar cells," *J. Mater. Chem. A* **4**, 17623 (2016).
- <sup>39</sup>H. Tan, A. Jain, O. Voznyy, X. Lan, F. P. G. de Arquer, J. Z. Fan, R. Quintero-Bermudez, M. Yuan, B. Zhang, Y. Zhao, F. Fan, P. Li, L. N. Quan, Y. Zhao, Z.-H. Lu, Z. Yang, S. Hoogland, and E. H. Sargent, "Efficient and stable solution-processes planar perovskite solar cells via contact passivation," *Science* **355**, 722

- (2017).
- <sup>40</sup>A. Cicciolelli and A. Latini, “Thermodynamics and the intrinsic stability of lead halide perovskites  $\text{CH}_3\text{NH}_3\text{PbX}_3$ ,” *J. Phys. Chem. Lett.* **9**, 3756 (2018).
- <sup>41</sup>W. Gao, C. Ran, J. Li, H. Dong, L. Zhang, X. Lan, X. Hou, and Z. Wu, “Robust stability of efficient lead-free formamidinium tin iodide perovskite solar cells realized by structural regulation,” *J. Phys. Chem. Lett.* **9**, 6999 (2018).
- <sup>42</sup>J.-P. Correa-Baena, A. Abate, M. Saliba, W. Tress, T. J. Jacobsson, M. Grätzel, and A. Hagfeldt, “The rapid evolution of highly efficient perovskite solar cells,” *Energy Environ. Sci.* **10**, 710 (2017).
- <sup>43</sup>A. M. Ganose, C. N. Savory, and D. O. Scanlon, “Beyond methylammonium lead iodide: prospects for the emergent field of  $\text{ns}^2$  containing solar absorbers,” *Chem. Commun.* **53**, 20 (2017).
- <sup>44</sup>J. Haruyama, K. Sodeyama, L. Han, and Y. Tateyama, “Termination dependence of tetragonal  $\text{CH}_3\text{NH}_3\text{PbI}_3$  surfaces for perovskite solar cells,” *J. Phys. Chem. Lett.* **5**, 2903–2909 (2014).
- <sup>45</sup>J. Haruyama, K. Sodeyama, L. Han, and Y. Tateyama, “Surface properties of  $\text{CH}_3\text{NH}_3\text{PbI}_3$  for perovskite solar cells,” *Acc. Chem. Res.* **49**, 554–561 (2016).
- <sup>46</sup>A. Akbari, J. Hashemi, E. Mosconi, F. D. Angelis, and M. Hakala, “First principles modelling of perovskite solar cells based on  $\text{TiO}_2$  and  $\text{Al}_2\text{O}_3$ : stability and interfacial electronic structure,” *J. Mater. Chem. A* **5**, 2339 (2017).
- <sup>47</sup>L. Zhang, X. Liu, J. Su, and J. Li, “First-principles study of molecular adsorption on lead iodide perovskite surface: A case study of halogen bond passivation for solar cell application,” *J. Phys. Chem. C* **120**, 23536–23541 (2020).
- <sup>48</sup>S. Wang, W. bo Xiao, and F. Wang, “Structural, electronic, and optical properties of cubic formamidinium lead iodide perovskite: a first-principles investigation,” *RSCA* **10**, 32364 (2020).
- <sup>49</sup>J. Xue, J.-W. Lee, Z. Dai, R. Wang, S. Nuryeva, S.-Y. C. Michael E. Liao, L. Meng, D. Meng, P. Sun, O. Lin, M. S. Goorsky, and Y. Yang, “Surface Ligand Management for Stable  $\text{FAPbI}_3$  Perovskite Quantum Dot Solar Cells,” *Joule* **2**, 1866 (2018).
- <sup>50</sup>Y. Fu, T. Wu, J. Wang, J. Zhai, M. J. Shearer, Y. Zhao, R. J. Hamers, E. Kan, K. Deng, X.-Y. Zhu, and S. Jin, “Stabilization of the metastable lead iodide perovskite phase via surface functionalization,” *NL* **17**, 4405 (2017).
- <sup>51</sup>Q. Jiang, Y. Zhao, X. Zhang, X. Yang, Y. Chen, Z. Chu, Q. Ye, X. Li, Z. Yin, and J. You, “Surface passivation of perovskite film for efficient solar cells,” *Nat. Photon.* **13**, 460 (2019).
- <sup>52</sup>P. Chen, Y. Bai, S. Wang, M. Lyu, J.-H. Yun, and L. Wang, “In Situ Growth of 2D Perovskite Capping Layer for Stable,” *Adv. Funct. Mater.* **28**, 1706923 (2018).
- <sup>53</sup>H. Cho, A. M. Soufiani, J. S. Yun, J. Kim, D. S. Lee, J. Seidel, X. Deng, M. A. Green, S. Huang, and A. W. Y. Ho-Baillie, “Mixed 3D–2D Passivation Treatment for Mixed-Cation Lead Mixed-Halide Perovskite Solar Cells for Higher Efficiency and Better Stability,” *Adv. Energy Mater.* **8**, 1703392 (2018).
- <sup>54</sup>M. Saliba, T. Matsui, J.-Y. Seo, K. Domanski, J.-P. Correa-Baena, M. K. Nazeeruddin, S. M. Zakeeruddin, W. Tress, A. Abate, A. Hagfeldt, and M. Grätzel, “Cesium-containing triple cation perovskite solar cells: Improved stability, reproducibility and high efficiency,” *Energy Environ. Sci.* **9**, 1989 (2016).
- <sup>55</sup>M. Saliba, S. Orlandi, T. Matsui, S. Aghazada, M. Cavazzini, J.-P. Correa-Baena, P. Gao, R. Scopelliti, E. Mosconi, K.-H. Dahmen, F. D. Angelis, A. Abate, A. Hagfeldt, G. Pozzi, M. Grätzel, and M. K. Nazeeruddin, “A molecularly engineered hole-transporting material for efficient perovskite solar cells,” *Nat. Energy* **1**, 15017 (2016).
- <sup>56</sup>M. Saliba, T. Matsui, K. Domanski, J.-Y. Seo, A. Ummadisingu, S. M. Zakeeruddin, J.-P. Correa-Baena, W. Tress, A. Abate, A. Hagfeldt, and M. Grätzel, “Entropic stabilization of mixed A-cation  $\text{ABX}_3$  metal halide perovskites for high performance perovskite solar cells,” *Science* **354**, 206 (2016).
- <sup>57</sup>L. Qiu, S. He, L. K. Ono, and Y. Qi, “Progress of Surface Science Studies on  $\text{ABX}_3$ -Based Metal Perovskite Solar Cells,” *Adv. Energy Mater.* **10**, 1902726 (2020).
- <sup>58</sup>J. He, D. Casanova, W.-H. Fang, R. Long, and O. V. Prezhdo, “Moiety termination favours efficient hole extraction and slow charge recombination at the  $\text{mapbI}_3/\text{cuscN}$  heterojunction,” *J. Chem. Phys.* **111**, 4481 (2020).
- <sup>59</sup>A. Seidu, M. Dvorak, P. Rinke, and J. Li, “Atomic and electronic structure of cesium lead triiodide surfaces,” *J. Chem. Phys.* **153**, 074712 (2021).
- <sup>60</sup>K. Reuter and M. Scheffler, “First-principles atomistic thermodynamics for oxidation catalysis: Surface phase diagrams and catalytically interesting regions,” *Phys. Rev. Lett.* **90**, 0461031 (2003).
- <sup>61</sup>Karsten Reuter and Catherine Stampfl and Matthias Scheffler, *Handbook of Material Modeling*, s. yip ed. (Springer Dordrecht, 2005) p. 149.
- <sup>62</sup>K. Reuter and M. Scheffler, “Composition and structure of the  $\text{ruo}_2(110)$  surface in an  $\text{o}_2$  and  $\text{co}$  environment: Implications for the catalytic formation of  $\text{co}_2$ ,” *Phys. Rev. B* **68**, 045407 (2003).
- <sup>63</sup>J. P. Perdew, A. Ruzsinszky, G. I. Csonka, O. A. Vydrov, G. E. Scuseria, L. A. Constantin, X. Zhou, and K. Burke, “Restoring the density-gradient expansion for exchange in solids and surfaces,” *Phys. Rev. Lett.* **100**, 136406 (2008).
- <sup>64</sup>V. Blum, R. Gehrke, F. Hanke, P. Havu, V. Havu, X. Ren, K. Reuter, and M. Scheffler, “*Ab initio* molecular simulations with numeric atom-centered orbitals,” *Comput. Phys. Commun.* **180**, 2175 (2009).
- <sup>65</sup>V. Havu, V. Blum, P. Havu, and M. Scheffler, “Efficient  $O(N)$  integration for all-electron electronic structure calculation using numeric basis functions,” *J. Comput. Phys.* **228**, 8367 (2009).
- <sup>66</sup>S. V. Levchenko, X. Ren, J. Wierferink, R. Johanni, P. Rinke, V. Blum, and M. Scheffler, “Hybrid functionals for large periodic systems in an all-electron, numeric atom-centered basis framework,” *Comput. Phys. Commun.* **192**, 60–69 (2015).
- <sup>67</sup>R. X. Yang, J. M. Skelton, E. L. da Silva, J. M. Frost, and A. Walsh, “Spontaneous octahedral tilting in the cubic inorganic cesium halide perovskites  $\text{CsSnX}_3$  and  $\text{CsPbX}_3$  ( $x = \text{f, cl, br, i}$ ),” *J. Phys. Chem. Lett.* **8**, 4720 (2017).
- <sup>68</sup>M. Bokdam, J. Lahnsteiner, B. Ramberger, T. Schäfer, and G. Kresse, “Assessing density functionals using many body theory for hybrid perovskites,” *Phys. Rev. Lett.* **119**, 145501 (2017).
- <sup>69</sup>E. van Lenthe, E. J. Baerends, and J. G. Snijders, “Relativistic regular two-component Hamiltonians,” *J. Chem. Phys.* **99** (1993).
- <sup>70</sup>F. Knuth, C. Carbogno, V. Atalla, V. Blum, and M. Scheffler, “All-electron formalism for total energy strain derivatives and stress tensor components for numeric atom-centered orbitals,” *Comput. Phys. Commun.* **190**, 33 (2015).
- <sup>71</sup>J. Neugebauer and M. Scheffler, “Adsorbate-substrate and adsorbate-adsorbate interactions of  $\text{Na}$  and  $\text{K}$  adlayers on  $\text{Al}(111)$ ,” *Phys. Rev. B* **46**, 16067 (1992).
- <sup>72</sup>L. Himanen, A. Geurts, A. S. Foster, and P. Rinke, “Data-driven materials science: Status, challenges, and perspectives,” *Adv. Sci.* **6**, 1900808 (2019).
- <sup>73</sup>include NOMAD link here.
- <sup>74</sup>C. C. Stoumpos, C. D. Malliakas, and M. G. Kanatzidis, “Semiconducting tin and lead iodide perovskites with organic cations: Phase transitions, high mobilities, and near-infrared photoluminescent properties,” *Inorg. Chem.* **52**, 9019–9038 (2013).
- <sup>75</sup>T. Baikie, Y. Fang, J. M. Kadro, M. Schreyer, F. Wei, S. G. Mhaisalkar, M. Grätzel, and T. J. White, “Synthesis and crystal chemistry of the hybrid perovskite  $(\text{CH}_3\text{NH}_3)\text{PbI}_3$  for solid-state sensitised solar cell applications,” *J. Mater. Chem. A* **1** (2013).
- <sup>76</sup>J. Lahnsteiner, G. Kresse, A. Kumar, D. D. Sarma, C. Francini, and M. Bokdam, “Room-temperature dynamic correlation between methylammonium molecules in lead-iodine based perovskites: An *ab initio* molecular dynamics perspective,” *Phys. Rev. B* **94**, 214114 (2016).

- <sup>77</sup>J. Li, J. Järvi, and P. Rinke, “Multiscale model for disordered hybrid perovskites: The concept of organic cation pair modes,” *Phys. Rev. B* **98**, 045201 (2018).
- <sup>78</sup>P. Schulz, D. Cahen, and A. Kahn, “Halide perovskites: Is it all about the interfaces?” *Chem. Rev.* , 3349 (2019).
- <sup>79</sup>V. Roiati, E. Mosconi, A. Listorti, S. Colella, iuseppe Gigli, and F. D. Angelis, “Stark Effect in Perovskite/TiO<sub>2</sub> Solar Cells: Evidence of Local Interfacial Order,” *Nano Lett.* **14**, 2168 (2014).
- <sup>80</sup>C. Caddeo, A. Filippetti, A. Filippetti, and A. Mattoni, “The dominant role of surfaces in the hysteretic behavior of hybrid perovskites,” *Nano Energy* **67**, 104162 (2020).
- <sup>81</sup>T. Baikie, Y. Fang, J. M. Kadro, M. Schreyer, F. Wei, S. G. Mhaisalkar, M. Graetzel, and T. J. White, “Synthesis and crystal chemistry of the hybrid perovskite (CH<sub>3</sub>NH<sub>3</sub>)PbI<sub>3</sub> for solid-state sensitised solar cell applications,” *J. Mater. Chem. A* **1**, 5628 (2013).
- <sup>82</sup>A. Mirzehmet, T. Ohtsuka, S. A. A. Rahman, T. Yuyama, P. Kruger, and H. Yoshida, “Surface termination of solution-processed ch<sub>3</sub>nh<sub>3</sub>pbi<sub>3</sub> perovskite film examined using electron spectroscopy,” *Adv. Mater.* **33** (2021).
- <sup>83</sup>W. Geng, C.-J. Tong, Z.-K. Tang, C. Yam, Y.-N. Zhang, W.-M. Lau, and L.-M. Liu, “Effect of surface composition on electronic properties of methylammonium lead iodide perovskite,” *Journal of Materiomics* **1**, 213 (2015).
- <sup>84</sup>J. Li and P. Rinke, “Atomic structure of metal-halide perovskites from first-principles: The chicken-and-egg paradox of the organic-inorganic interactions,” *Phys. Rev. B* **94**, 045201 (2016).
- <sup>85</sup>J. Li, M. Bouchard, P. Reiss, D. Aldakov, S. Pouget, R. Demadrille, C. Aumaitre, B. Frick, D. Djurado, M. Rossi, , and P. Rinke, “Activation energy of organic cation rotation in CH<sub>3</sub>NH<sub>3</sub>PbI<sub>3</sub> and CD<sub>3</sub>NH<sub>3</sub>PbI<sub>3</sub>: Quasi-elastic neutron scattering measurements and first-principles analysis including nuclear quantum effects,” *J. Phys. Chem. Lett.* **9**, 3969 (2018).